Received: 16 April 2019 | Revised: 2 October 2020 | Accepted: 13 April 2021
DOI: 10.1002/stc.2773

RESEARCH ARTICLE

WILEY

Bridge scour characteristic curve for natural frequency-based bridge scour monitoring using simulation-based optimization

Ting Bao[1,2,3] | **Zhen (Leo) Liu**[3]

[1]School of Civil Engineering, Chongqing University, Chongqing, China
[2]Key Laboratory of New Technology for Construction of Cities in Mountain Area, Chongqing University, Chongqing, China
[3]Department of Civil and Environmental Engineering, Michigan Technological University, Houghton, MI, USA

Correspondence
Ting Bao, Department of Civil and Environmental Engineering, Michigan Technological University, 1400 Townsend Drive, Dow 854, Houghton, MI 49931, USA.
Email: tbao@mtu.edu

Summary
This study addresses a key issue that prevents the wide application of the novel predominant natural frequency (PNF)-based method for bridge scour monitoring, which is also applicable to the frequency-based health monitoring of other structures with soil–structure interaction. This issue is that no theory or method is currently available to guide the prediction of scour depths based on measured PNFs. The most feasible way is to first measure a few scour depths and their corresponding PNFs for obtaining the PNF–scour depth relationship, which is termed the bridge scour characteristic curve (BSCC) in this study, and then use this BSCC to predict future scour depths with measured PNFs. This study provides a comprehensive investigation into the BSCC and proposes a simulation-based optimization approach, in which the whole BSCC, that is, from light to severe scour conditions, can be predicted with a few measured scour depth–PNF data points (e.g., 2–4) within a small scour depth range (e.g., 0.2–0.5 m). The proposed approach integrates the Winkler-based numerical model into a global optimization technique to predict the whole BSCC to avoid the use of a closed-form BSCC function, which may not exist. Additionally, the approach can be used to estimate the modulus of subgrade reaction, which is very hard to obtain at real bridges. The performance of the proposed approach was evaluated using several practical scenarios with realistic multi-layered soil conditions. We found that the proposed approach is accurate for predicting the whole BSCC with four measured points or even less, regardless of the scour severity for the measurements and the number of the soil layer. For applications, the influence of random errors in the measurements of PNFs and scour depths was investigated and concluded to be negligible. This study sets a solid cornerstone for the maturation of the PNF-based scour monitoring method and other frequency-based structural health monitoring methods with soil–structure interaction.

KEYWORDS
bridge scour characteristic curve, predominant natural frequency, scour detection, simulation-based optimization, soil–structure interaction

1 | INTRODUCTION

Bridge scour involves the erosion of soils around the foundations of bridge piers or abutments due to moving water, especially rapid flows during floods and rainstorms. Statistics indicates that scour is one of the major causes of bridge failures in the United States.[1–3] Over 20,000 bridges in the United States are in danger of failures resulting from bridge scour according to Gee[4] and Yu et al.[5] Other statistics shows that 58% of 1502 reported bridge failures during 1966–2005 were caused by bridge scour.[6] Therefore, numerous research efforts have been made to develop useful techniques for detecting bridge scour.

Among these efforts, vibration-based scour detection has been gaining momentum.[7] The presence of scour alters the vibration characteristics of bridges/bridge piers due to the stiffness reduction caused by scour. Scour thus can be detected using the modal analysis of bridges/bridge piers. Significant changes in horizontal modal displacements[8] and modal shapes[9] can be induced if scour develops, because scour removes soils around bridge foundations to lose the support. One also can use other modal parameters to detect scour, including the damage factor of modal shape curvatures,[7,9] modal assurance criterion,[10] and flexibility-based deflections.[9,10] However, to accurately evaluate the above modal parameters for scour detection, several sensors and/or numerical simulations of bridges are needed, which makes scour detection in practice demanding in real-time monitoring. A novel method of utilizing the predominant natural frequency (PNF) of a bridge pier has been attracting increasing attention recently as this method is relatively less demanding and can avoid difficulties in installing underwater instruments on or near bridges or bridge foundations, which are needed in other conventional techniques.[5,11–16] Instead, as shown in Figure 1, an accelerometer is installed on the top of a bridge pier to collect the pier's dynamic responses[7] for scour monitoring. The hypothesis for this method is that scour development reduces the stiffness of a bridge pier and thus decreases the PNF of that pier, which has been verified by both numerical studies[17–20] and experimental studies.[21–23]

The effectiveness of PNF-based scour monitoring has also been discussed to advance this novel method. One practical concern is how to vibrate a bridge pier for generating valid dynamic signals for data postprocessing to obtain the PNF of the test pier. Experimental studies[21,24] have successfully generated vibration using ambient vibration measurements, such as rapid flows. The effectiveness of this novel method has also been confirmed with complex field conditions, for example, different types of foundations,[19,21] fluid–structure interaction,[20] and both clayey and sandy soils.[25] In addition, numerical results have verified the feasibility of the method for full-scale bridges, for example, Zhang et al.[19] and Ju,[20] and even for a more complicated cable-stayed bridge.[26] Besides, Li et al.[27] confirmed that

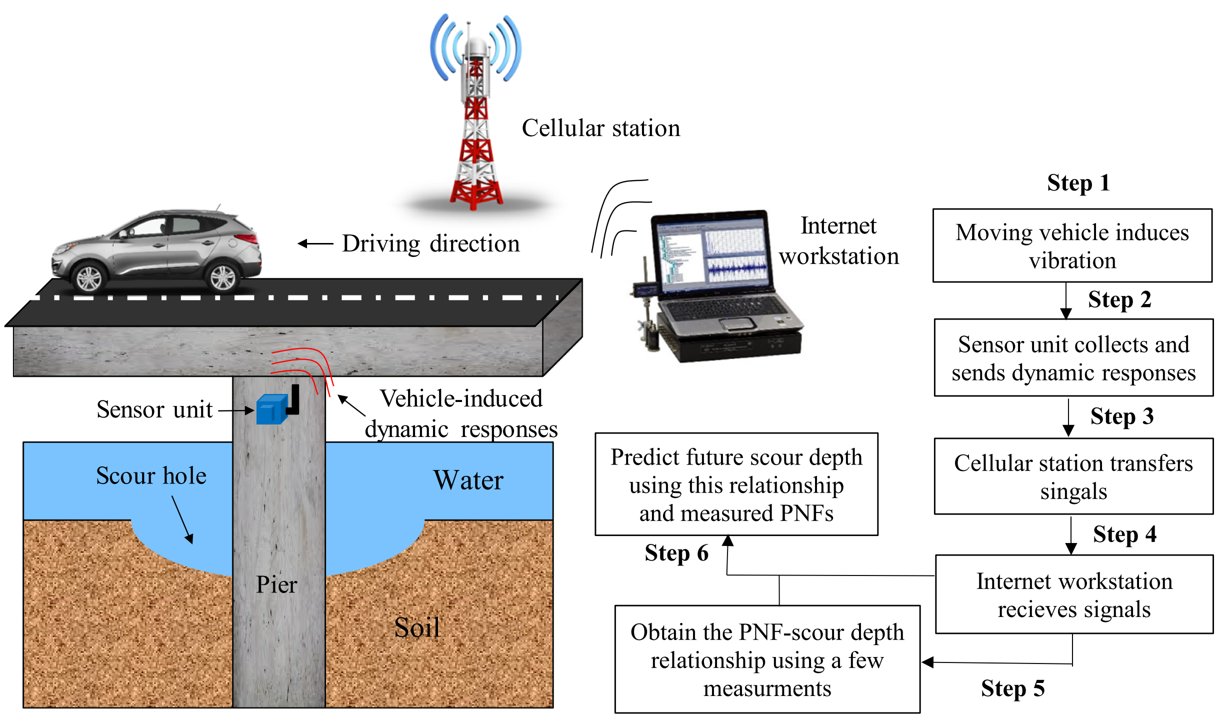

FIGURE 1 Conceptual schematic and workflow of PNF-based scour monitoring

environmental influences on the PNF can be reduced using the nonlinear principal component analysis. This may help improve the quality of signals picked up in fields for obtaining the PNF.

Despite the above progress, the application of PNF-based scour monitoring at real bridges still far lags behind. Two unresolved critical questions hinder the application of this novel method in practice. The first question is "whether a change caused by progressive scour in the PNF of a bridge/bridge pier is significant enough to be identified in field measurements?" A minor variation in the PNF caused by scour may render this method infeasible in the field. Also, environmental factors, such as moving vehicles and winds, may also lead to failures in the PNF measurement. The recent results reported by Prendergast et al.[28] showed that the magnitude of changes in the PNF is sufficiently large for scour severity monitoring and also confirmed that moving vehicles can generate realistic dynamic signals for obtaining the PNF. Therefore, Steps 1–4 in the conceptual framework of this novel method (see Figure 1) have become feasible by utilizing moving vehicles for vibration and a wireless technique for signal transmission. However, despite the above advances, we believe that a solid answer to this question still needs more field tests on real bridge piers to consider the influence of environmental factors and more studies on the acquisition of the PNF with results from these field tests.

The second critical question is "how can we predict future scour depths with measured PNFs?" This second question is essential to the implementation of this scour detection method. Since it is difficult to directly measure scour depths at real bridges, the most feasible way is to first measure a few scour depths and their corresponding PNFs for obtaining the PNF–scour depth relationship (Step 5) and then use later measured PNFs for scour depth predictions based on this relationship (Step 6). Therefore, an in-depth understanding of the PNF–scour depth relationship and the accurate prediction of this relationship become a key to enabling the wide application of the PNF-based method in practice. Especially, it is advantageous and highly desirable to accurately predict this relationship with only a few measured data points (e.g., 2–4). However, rare research has been reported on addressing this need.

To fill this critical knowledge gap, we propose a novel simulation-based optimization approach to predict the PNF–scour depth relationship with 2–4 field measurements. First, the PNF–scour depth relationships, which are termed the bridge scour characteristic curve (BSCC) here, are summarized and discussed with existing numerical and experimental studies to reveal the characteristics of the BSCC. After that, a detailed Winkler-based numerical model and its implementation are presented and then validated against a documented test. Next, a simulation-based optimization approach is introduced, which integrates the Winkler-based numerical model into a global optimization technique to predict the whole BSCC. Finally, the performance of the proposed approach for predicting the whole BSCC with four measured data points in multilayered soil conditions is assessed. The influences of the number of measured data points and errors in field measurements on the accuracy of the BSCC prediction are also investigated.

2 | THEORY AND SIMULATION

2.1 | Bridge scour characteristic curve

The BSCC serves as the major constitutive relationship in PNF-based scour detection, which is similar to the role of the soil water characteristic curve (SWCC) in the application of unsaturated soil mechanics.[29,30] To evaluate the BSCC, this section summarizes and discusses the PNF–scour depth data from existing numerical and experimental studies. The results can be classified into two types based on the shape of the BSCC. The first type is associated with 3D simulations employing the PNF of a bridge (Figure 2a,b), which contain the soil mass and fluid–structure interaction. The second type is found in an experimental study of an open-ended pier and its sprung-beam model simulations (Figure 2c) and in a numerical study of a vehicle–bridge–soil interaction (VBSI) model (Figure 2d), both of which neglect the soil mass.

As for the first type, the BSCCs obtained in the 3D numerical simulations of Huang et al.[31] and Zhang et al.[19] in Figure 2a are nonlinear, no matter the soil's elastic modulus increases or remains unchanged with depths. The 3D simulation results obtained from Ju[20] involving the fluid–structure interaction also yielded nonlinear BSCCs (Figure 2b). The nonsmooth BSCCs are due to nonuniformly layered soils around the foundations.[20] As for the second type, as shown in Figure 2c, the BSCC from the field study in Prendergast et al.[22] is nonlinear. Nonlinear BSCCs were also obtained in the sprung-beam model simulations to simulate the field test in the same study,[22] which employed three methods (shear wave, CPT, and API) to approximate the lateral stiffness of soils. The VBSI simulation results from Prendergast et al.[28] confirmed the nonlinearity of BSCCs (Figure 2d). Based on the above results, we conclude that the BSCC is nonlinear.

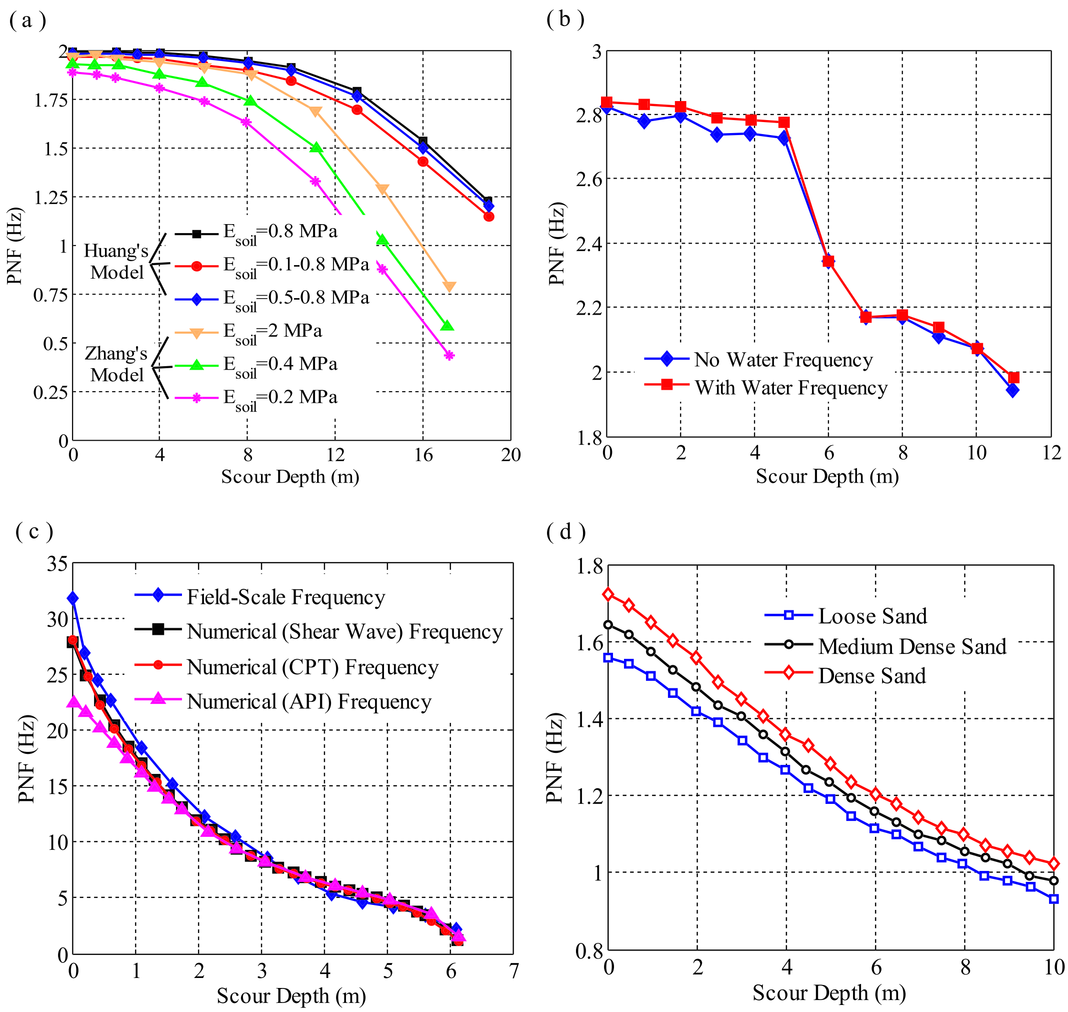

FIGURE 2 Relationships between the PNF and scour depth: (a) Huang et al.[31] and Zhang et al.,[19] (b) Ju,[20] (c) Prendergast et al.,[22] and (d) Prendergast et al.[28]

These two types of nonlinear BSCCs exhibit different shapes. More specifically, the BSCCs from the 3D simulations of whole bridges are convex with progressive scour, whereas those from the sprung-beam simulations of single piers are concave. The reason is that a pier is only a small component of a bridge. Accordingly, the same scour depth will induce a less significant change in the PNF of a bridge than that of a pier of that bridge, because the scour-induced stiffness decrease is more obvious in the local component (i.e., the pier) than the bridge, which is also supported by other components. From a practical viewpoint, a more significant decrease is more useful to the application of this method. This is because the greater the decrease in the stiffness, the more likely the change in the PNF can be detected. Therefore, a pier is preferable to a bridge from this perspective. Another advantage of using the PNF of a pier is that only one accelerometer is needed to be installed on the pier, whereas multiple sensors are needed for a bridge. The signals measured by the accelerometer mainly stand for the dynamic responses of that pier rather than the entire structure of the bridge.

2.2 | Theoretical model and implementation

In this section, a theoretical model of the BSCC of a single pier is presented based on the Winkler theory. We propose a numerical framework here to implement the model rather than use the commercial code with a purpose for obtaining fast solutions (within seconds) and flexibility in an automated sensitivity analysis. The efficiency and flexibility of the proposed model are needed for the following simulation-based optimization for predicting the BSCC. The numerical solutions serve as a mapping from inputs, for example, soil properties, to outputs, for example, BSCCs. This mapping replaces the role of mathematical functions in conventional curve fitting processes. In addition, unlike most previous studies with the finite element method, for example, Prendergast et al.,[22] the numerical model developed in this section will be discretized and solved with the finite difference method by coding using MATLAB. The procedure for numerically implementing the model will also be detailed, such that the results presented in this study could be easily reproduced. The detail of the model and its implementation is introduced in the following.

A bridge pier with a deck partially embedded in a soil can be simplified as a beam-elastic foundation model,[32,33] in which the lumped mass on the top of that beam is used to represent the superstructure.[34] According to Wang et al.,[35] the motion of a beam fully embedded in a semi-infinite linearly elastic medium satisfies

$$m\ddot{u}+c\dot{u}+EIu''''-j\ddot{u}''+k_0u= p_d-\underbrace{\frac{h}{2}(u'k_0u)'}_{\text{quadratic nonlinear term}}\underbrace{-EI\left[u'(u'')^2+(u')^2u'''\right]'}_{\text{cubic nonlinear term}}-\underbrace{\left[\frac{u'}{2}\int_l^x m\frac{\partial^2}{\partial t^2}\int_0^x (u')^2dxdx\right]'}_{\text{cubic nonlinear term}} \tag{1}$$

where u is the lateral deflection (m); $\dot{u}$ and u' denote the first derivatives of u with respect to time and the spatial coordinate (along the axis of the beam), respectively; m is the mass per unit length (kg/m) for the beam with the same cross section; p_d is the external distributed load (N/m); c is the damping; EI is the flexural rigidity of the beam (kN/m^2); $j=\int_{A_c}\rho_b y^2 dA_c$ is the rotary inertia, in which A_c is the cross-sectional area of the beam (m^2), and ρ_b is the beam density (kg/m^3); and k_0 is the modulus of subgrade reaction (N/m^2). The three right-most terms on the right-hand side of Equation 1 are nonlinear terms.

Equation 1 excludes the fluid–beam interaction. This exclusion is reasonable because Ju[20] confirmed that the difference between the PNFs calculated with water and without water is negligible (Figure 2b). The soil-pier interaction in Equation 1 is formulated using the Winkler theory, which has been widely used in foundation engineering practice.[36–38] The hypothesis of the Winkler theory is that, as shown in Figure 3, the soil can be represented using a series of unconnected and concentrated springs perpendicular to the pier.[37] A test pier embedded in a soil is modeled using a series of beam elements. The bridge deck is formulated with a lumped mass on the top.

If we neglect all nonlinear, high-order, damping and external load terms, Equation 1 can be simplified into

$$m\ddot{u}+EIu''''-j\ddot{u}''+k_0u=0. \tag{2}$$

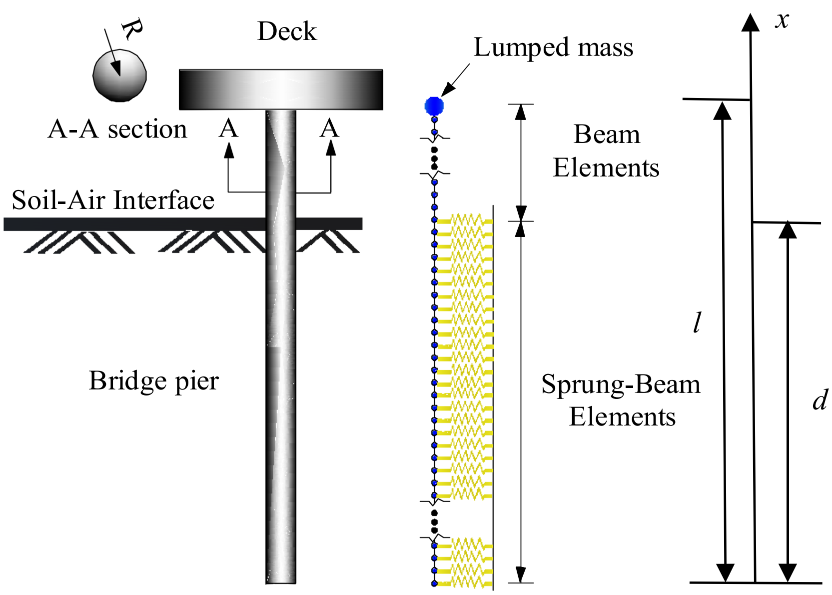

FIGURE 3 Schematic of the beam-elastic foundation model with lumped mass

Equation 2 describes the linearly undamped free vibration of a beam fully embedded in a semi-infinite linearly elastic medium. However, a real bridge pier is partially embedded in the ground. To account for this condition, Equation 2 is extended to a piecewise function as shown in Equations 3 and 4, in which k_0 only exists in the embedded part of the beam, because there is no interaction between the exposed part of the beam and the soil:

$$m\ddot{u} + EIu'''' - j\ddot{u}'' = 0 \quad d \le x \le l, \tag{3}$$

$$m\ddot{u} + EIu'''' - j\ddot{u}'' + k_0 u = 0 \quad 0 \le x \le d, \tag{4}$$

where d and l are the embedded length (m) and the total length (m) of the beam (see Figure 3), respectively. To obtain the PNF of the beam, the modal analysis was conducted using Equations 3 and 4. This analysis is equivalent to the natural frequency spectrum analysis of dynamic data measured at the beam. The general solution to this motion equation can be assumed of the form, $u = Ue^{i\omega t}$, where ω is the angular natural frequency of the beam and U is the modal shape function. Substituting this general solution into Equations 3 and 4, we obtain

$$EIU'''' + j\omega^2 U'' - m\omega^2 U = 0 \quad d \le x \le l, \tag{5}$$

$$EIU'''' + j\omega^2 U'' + \left(k_0 - m\omega^2\right) U = 0 \quad 0 \le x \le d. \tag{6}$$

For convenience, the above piecewise equations are rewritten into a general form of eigenvalue problems:

$$V'''' + \omega^2 \left(\frac{j}{EI} V'' - \frac{m}{EI} V\right) = 0, \tag{7}$$

$$U'''' + \frac{k_0}{EI} U + \omega^2 \left(\frac{j}{EI} U'' - \frac{m}{EI} U\right) = 0, \tag{8}$$

where U is the modal shape function for the embedded part and V is the modal shape function for the exposed part. Once ω is calculated as the solution to the above eigenvalue problem with specified boundary conditions, the natural frequency of the beam, f, can be simply computed using $f = \omega/2\pi$. The boundary conditions for the pier shown in Figure 3 are formulated as

$$\text{Exposed part} \begin{cases} V''|_{x=l} = 0, \\ V'''|_{x=l} = 0, \end{cases} \tag{9}$$

$$\text{Continuous part} \begin{cases} U|_{x=d} = V|_{x=d}, \\ U'|_{x=d} = V'|_{x=d}, \\ U''|_{x=d} = V''|_{x=d}, \\ U'''|_{x=d} = V'''|_{x=d}, \end{cases} \tag{10}$$

$$\text{Embedded part} \begin{cases} U''|_{x=0} = 0, \\ U'''|_{x=0} = 0. \end{cases} \tag{11}$$

Equations 7 and 8 with boundary conditions in Equations 9–11 were discretized and solved using the finite difference method.

Substituting Taylor series expansion approximations (see Equations A1 and A2) into Equation 7, we obtain a system of linear equations:

$$\left(C + \omega^2 D\right)\{V\} = 0, \tag{12}$$

where C and D are tridiagonal matrices, and $\{V\}=[V_1, V_2, ..., V_i]^T$, in which i is the maximum index of V. A similar procedure can be taken to obtain another system of linear equations for U in the soil:

$$\left(A+\omega^2 B\right)\{U\}=0, \tag{13}$$

where A and B are tridiagonal matrices, and $\{U\}=[U_{i+1}, U_{i+2}, ..., U_{n-1}, U_n]^T$, in which n is the sum of the maximum indices of V and U.

The incorporation of the boundary conditions formulated by Equations 9–11 into Equations 12 and 13 is crucial in the discretization. Equation 12 includes the second and third derivatives of V. By applying the Taylor series expansion for V to Equation 9 and then substituting the discretized form of Equation 9 into Equation 12, we obtain the matrix formulation for the exposed part of the beam:

$$\left(\begin{bmatrix} 1 & -2 & 1 & 0 & \cdots & 0 \\ -2 & 5 & -4 & 1 & \cdots & 0 \\ 1 & -4 & 6 & -4 & \ddots & 0 \\ 0 & 1 & -4 & 6 & \ddots & 1 \\ \vdots & \vdots & \ddots & \ddots & \ddots & -4 \\ 0 & 0 & 0 & 1 & -4 & 6 \end{bmatrix} + \omega^2 \begin{bmatrix} 2CC+DD & 0 & 0 & \cdots & 0 & 0 \\ CC & DD & CC & \cdots & 0 & 0 \\ 0 & CC & DD & \ddots & 0 & 0 \\ 0 & 0 & CC & \ddots & CC & \vdots \\ \vdots & \vdots & \ddots & \ddots & DD & CC \\ 0 & 0 & 0 & 0 & CC & DD \end{bmatrix}\right) \begin{bmatrix} V_1 \\ V_2 \\ V_3 \\ \vdots \\ V_{i-1} \\ V_i \end{bmatrix} = \mathbf{0}, \tag{14}$$

where $CC=\Delta x^2 j/EI$ and $DD=-(\Delta x^4 m+2\Delta x^2 j)/EI$. Similarly, the boundary condition formulated by Equation 11 can be incorporated into Equation 13 to obtain the matrix formulation for the embedded part:

$$\left(\begin{bmatrix} BB & NN & 1 & 0 & \ldots & 0 \\ NN & BB & NN & 1 & \cdots & 0 \\ 1 & NN & \ddots & \ddots & \ddots & \vdots \\ \vdots & \ddots & \ddots & BB & NN & 1 \\ 0 & 0 & 1 & NN & BB-1 & 2+NN \\ 0 & 0 & 0 & 1 & -2 & BB+2NN+3 \end{bmatrix} + \omega^2 \begin{bmatrix} DD & CC & 0 & \cdots & 0 & 0 \\ CC & DD & CC & \cdots & 0 & 0 \\ 0 & CC & DD & \ddots & 0 & 0 \\ 0 & 0 & \ddots & \ddots & CC & \vdots \\ \vdots & \vdots & \ddots & CC & DD & CC \\ 0 & 0 & 0 & 0 & 0 & 2CC+DD \end{bmatrix}\right) \begin{bmatrix} U_{i+1} \\ U_{i+2} \\ U_{i+3} \\ \vdots \\ U_{n-1} \\ U_n \end{bmatrix} = \mathbf{0}, \tag{15}$$

where $BB = 6 + \Delta x^4 k_0 / EI$ and $NN = -4$. The real test pier needs to be continuous and smooth; therefore, the continuity between the exposed part and the embedded part needs to be ensured. For the purpose, the boundary condition in Equation 10 defines that the modal shape at the bottom of the exposed part, that is, V_i, is equal to that at the top of the embedded part, that is, U_{i+1}.

Two steps were taken to obtain the complete matrix of the system. The first step was to utilize the same coefficient in the matrix for variables in the lines of V_i and U_{i+1} to make $V_i = U_{i+1}$. Second, the coefficients of V_{i-1} and of U_{i+2} in the matrix were rearranged to avoid using V_i and U_{i+1} twice because $V_i = U_{i+1}$. The diagonal matrix of the whole system including the boundary conditions in Equations 9–11 is obtained as below:

$$
\left(
\begin{bmatrix}
1 & -2 & 1 & 0 & \ldots & 0 & \cdots & \cdots & \cdots & \cdots & \cdots & 0 \\
-2 & 5 & -4 & 1 & \cdots & 0 & \ddots & \ddots & \ddots & \ddots & \ddots & \vdots \\
1 & -4 & 6 & -4 & \ddots & 0 & \cdots & \ddots & \ddots & \ddots & \ddots & \vdots \\
0 & 1 & -4 & 6 & \ddots & 1 & 0 & \cdots & \ddots & \ddots & \ddots & \vdots \\
\vdots & \vdots & \ddots & \ddots & \ddots & -4 & 0 & 1 & 0 & \ddots & \ddots & \vdots \\
0 & 0 & 0 & 1 & NN & BB & 0 & NN & 1 & 0 & \ddots & 0 \\
0 & \cdots & 0 & 1 & NN & 0 & BB & NN & 1 & 0 & \cdots & 0 \\
0 & \ddots & \cdots & 0 & 1 & 0 & NN & BB & NN & 1 & \cdots & 0 \\
\vdots & \ddots & \ddots & \ddots & \ddots & \ddots & 1 & NN & \ddots & \ddots & \ddots & \vdots \\
\vdots & \ddots & \ddots & \ddots & \ddots & \ddots & \ddots & \ddots & \ddots & BB & NN & 1 \\
\vdots & \vdots & \ddots & \ddots & \ddots & \ddots & 0 & 0 & 1 & NN & BB-1 & 2+NN \\
0 & \cdots & \cdots & \cdots & \cdots & \cdots & 0 & 0 & 0 & 1 & -2 & BB+2NN+3
\end{bmatrix}
+ \right.
$$

$$
\left. \omega^2
\begin{bmatrix}
2CC+DD & 0 & 0 & \ldots & 0 & 0 & \cdots & \cdots & \cdots & \cdots & \cdots & 0 \\
CC & DD & CC & \ldots & 0 & 0 & \ddots & \ddots & \ddots & \ddots & \ddots & \vdots \\
0 & CC & DD & \ddots & 0 & \vdots & \ddots & \ddots & \ddots & \ddots & \ddots & \vdots \\
0 & 0 & CC & \ddots & CC & 0 & \ddots & \ddots & \ddots & \ddots & \ddots & \vdots \\
\vdots & \vdots & \ddots & \ddots & DD & CC & 0 & \ddots & \ddots & \ddots & \ddots & 0 \\
0 & 0 & 0 & 0 & CC & DD & 0 & CC & 0 & \ddots & \ddots & 0 \\
0 & \ddots & \cdots & 0 & CC & 0 & DD & CC & 0 & \ddots & \ddots & \vdots \\
\vdots & \ddots & \ddots & \ddots & 0 & 0 & CC & DD & CC & \ddots & \ddots & \vdots \\
\vdots & \ddots & \ddots & \ddots & \ddots & \ddots & 0 & CC & DD & \ddots & \ddots & \vdots \\
\vdots & \ddots & \ddots & \ddots & \ddots & \ddots & \ddots & 0 & \ddots & \ddots & CC & 0 \\
\vdots & \vdots & \ddots & \ddots & \ddots & \ddots & \ddots & \ddots & \ddots & CC & DD & CC \\
0 & \cdots & \cdots & \cdots & \cdots & \cdots & \cdots & \cdots & \cdots & 0 & 0 & 2CC+DD
\end{bmatrix}
\right)
\begin{bmatrix}
V_1 \\ V_2 \\ V_3 \\ \vdots \\ V_{i-1} \\ V_i \\ U_{i+1} \\ U_{i+2} \\ U_{i+3} \\ \vdots \\ U_{n-1} \\ U_n
\end{bmatrix}
= \mathbf{0}. \tag{16}
$$

The first primary eigenvalue of Equation 16 can be obtained as the PNF of the pier. The discretization and eigenvalue solutions were implemented with MATLAB. The validation of the model against documented measurements will be introduced in the following.

2.3 | Validation of numerical framework

The proposed numerical framework was validated against a documented test. Prendergast et al.[22] conducted a field test at a dense sand site to investigate the change in the PNF of a pier with progressive scour. The test pier is an open-ended steel pier partially embedded in a sand stratum. The in situ measured PNFs of this steel pier were utilized for the validation. The soil properties used in the simulations were obtained from Prendergast et al.[22] The lateral stiffness of the soil was derived from the small-strain stiffness method (SSSM; see Appendix A). This method was adopted in the current study because the comparison results[22,39] showed that the SSSM has better PNF predictions than the API *p–y* curve approach when compared to the experimental data. As shown in Figure 4, the Winkler-based PNFs computed using the proposed numerical framework are very close to the measured PNFs, which demonstrates the high accuracy of the proposed numerical framework. The experimental results in Figure 4 are the same as those plotted in Figure 2c. We also can see from Figures 2c and 4 that the computed PNFs in the current study via the finite difference method are close to PNFs computed by Prendergast et al.[22] via the finite element method. It is noted that the proposed numerical model in Section 2.2 is needed for the following simulation-based optimization approach for predicting the BSCC (see Figure 5), where the numerical solutions calculated by the proposed numerical model will serve as a mapping from inputs, for example, soil properties, to outputs, for example, BSCCs.

2.4 | Simulation-based optimization

Simulation-based optimization is the integration of numerical simulations into optimization techniques for predicting unknown parameters in the simulations.[40] In civil engineering, optimization can be integrated into simulations for predicting geotechnical parameters that are difficult to obtain via experiments[41,42] and can be utilized for identifying defects in structures for structural health monitoring.[43,44] A global optimization technique is needed when the behavior of a system is highly nonlinear, such as the BSCC. The global optimization technique adopted in this study is the multi-start method. This method will restart the search from a new solution once a region has been extensively explored.[45,46] The solution is improved in each restart process to find the global minimum of its objective function rather than the local minima according to specified criteria.[47] Mathematically, a global optimization problem with variable bound constraints can be expressed as

$$\min_{\mathbf{x} \in \vartheta} g(\mathbf{x}), \quad \vartheta \in R^n \text{ and } \mathbf{x}_u \geq \mathbf{x} \geq \mathbf{x}_l, \tag{17}$$

where $g(\mathbf{x})$ is the objective function, ϑ is the feasible domain, $\mathbf{x}_u$ and $\mathbf{x}_l$ are the upper and lower bounds in the feasible domain, and $\mathbf{x}$ is the vector within the bounds. If $g(\mathbf{x}_{\text{opt}}) \leq g(\mathbf{x}) \, \forall \, \mathbf{x} \in \vartheta$, $\mathbf{x}_{\text{opt}}$ is the global minimum of that objective

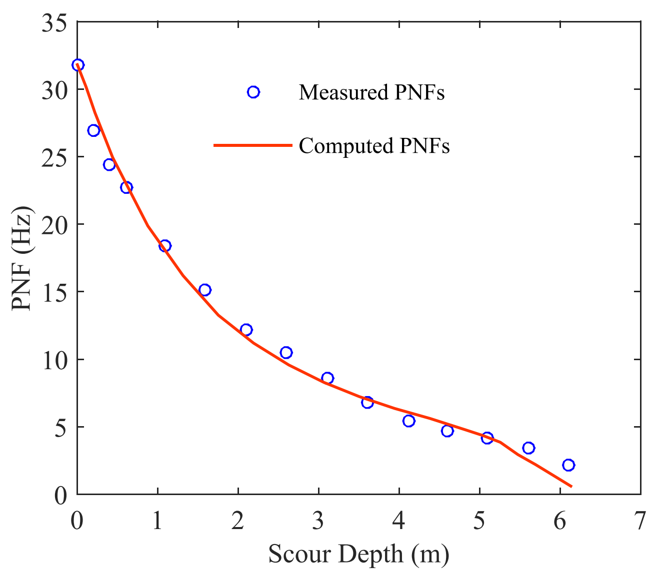

FIGURE 4 Comparison between PNFs computed by the proposed numerical model and PNFs measured by Prendergast et al.[22]

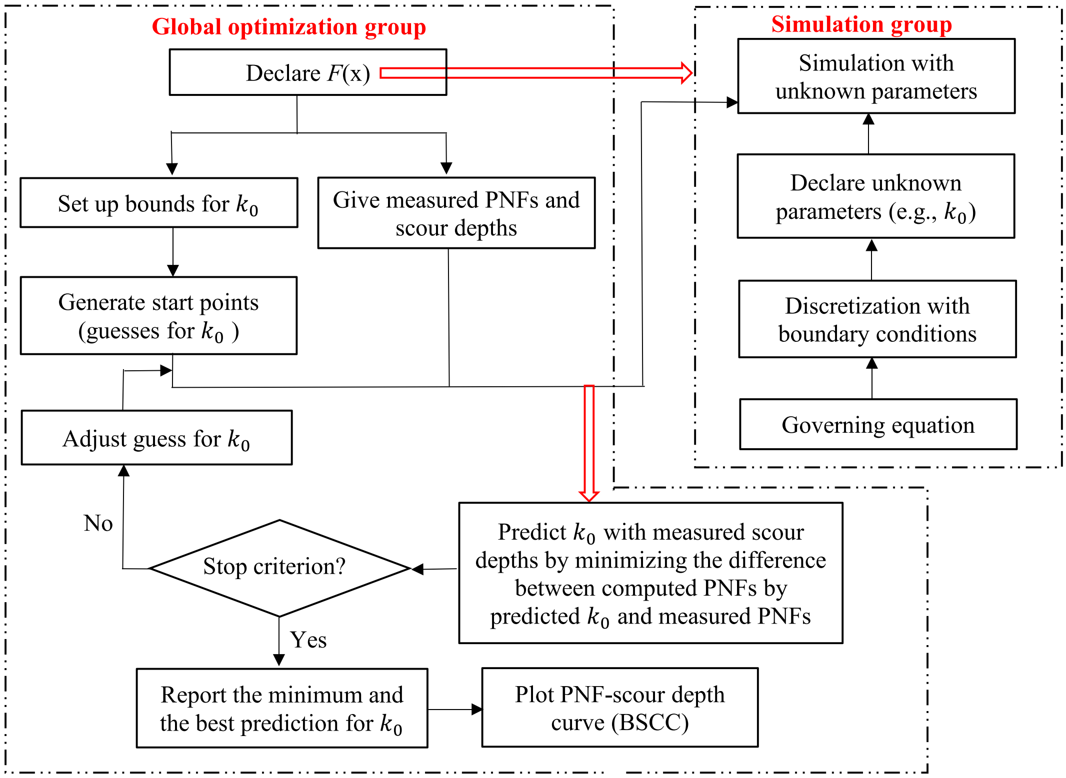

FIGURE 5 Flowchart of simulation-based optimization for BSCC prediction

function. In this global optimization technique, the nonlinear least-squares algorithm was adopted to calculate $g(\mathbf{x})$; therefore, $g(\mathbf{x}) = \sum (F(\mathbf{x}, \mathbf{x}\text{data}_i) - \mathbf{y}\text{data}_i)^2$, where **x**data is the input (e.g., k_0), **y**data is the output (e.g., BSCC), and $F(\mathbf{x})$ is the analytical curve fitting function.

Theoretical formulations for geotechnical problems, such as Equation 2, are usually highly nonlinear, leading to a difficulty in finding an analytical solution. Under this condition, no closed-form function is available for the direct acquisition of $F(\mathbf{x})$ used by $g(\mathbf{x})$ in this study. To address this issue, the numerical solution to Equation 16 with the proposed numerical framework (simulation group in Figure 5), which serves as $F(\mathbf{x})$, was implemented to predict the unknown parameters via optimization by minimizing the difference between predictions and measurements via the search of the best objective value in the optimization process. Preassumed values of the unknown parameters (e.g., k_0) were modified to approximate the true values in the global optimization process. The detailed process is introduced in the following.

The simulation-based optimization approach shown in Figure 5 starts with the simulation group (right), in which the governing equation together with the boundary conditions is discretized and the unknown parameters (e.g., k_0) are declared. The simulation group also requires the guesses from the global optimization technique as the input. In the global optimization group (right), the discretized form of the numerical model (i.e., simulation group) is then declared as $F(\mathbf{x})$. We also set up bounds and generate guesses for k_0. Simultaneously, we enter measured data points, that is, PNFs and scour depths. The initial or adjusted guess of k_0, depending on whether it is the initial run, is sent to the simulation group to compute PNFs under given measured scour depths. The computed PNFs by employing this initial/adjusted guess are compared with given measured PNFs. If the stop criterion is satisfied, the initial guess is the best prediction for k_0. Otherwise, the initial guess will be adjusted and sent to the simulation group again to search for a better prediction for k_0 by minimizing the difference between the computed PNFs (obtained by the adjusted guess of k_0) and the given measured PNFs. This process is repeated until the stop criterion is satisfied. At that time, the global minimum is found, and the corresponding guess of k_0 is the best prediction. With a very strict criterion, this best prediction can be deemed to be close to the true solution. Accordingly, the BSCC obtained with the above process is accepted as the real BSCC.

3 | RESULTS AND DISCUSSION

3.1 | Description of simulation-based optimization cases

This subsection describes the cases and assumptions for evaluating the performance of simulation-based optimization in predicting whole BSCCs. The system simulated by the numerical model consists of a pier and a superstructure on its top (see Figure 6) to model a simply supported beam bridge with a monopile foundation according to Mylonakis et al.[34] and Cao and Yuan.[48] A cylindrical pier was chosen because this type of pier has serious scour issues, for example, scour depth over 6 m, according to field measurements reported by Mueller and Wagner.[49] A pier diameter of 4.3 m and a length of 16.5 m were adopted based on the bridge pier cases in Mueller and Wagner.[49] The embedded length of the pier in the soil was selected to be 13 m to cover a large range of the PNF variation with scour depths according to the guide provided in CDOESTO.[50]

Physical soil and pier material properties used for simulation-based optimization are detailed in Figure 6. Multilayered soils were adopted to approximate realistic soil conditions according to Mylonakis et al.[34] and Ashford and Juirnarongrit.[51] Four scour cases from light to severe scour conditions in Figure 6 for four representative local scour depth ranges in the BSCC were considered. The modulus of subgrade reaction k_0 was declared as the unknown geotechnical parameter considering that k_0 is needed to calculate the soil stiffness (detailed in Appendix A) but very difficult to obtain at real bridges. EI and ρ_b needed for solving Equations 3 and 4 could usually be determined by checking bridge foundation design documents and thus are treated as known parameters in this study. Four measured scour depths and their corresponding PNFs are needed as the input. According to the strategy in Zhang et al.,[42] numerically computed PNFs with true k_0 (calculated with Equation A4 based on measured E_s in Table 2)[22] were treated as "measured PNFs" for each case in Table 1. Therefore, the measurement points are accurate, except for the computational truncation error.

3.2 | BSCC prediction with multilayered soils

The prediction of the whole BSCC with multilayered soil conditions is assessed in this subsection. The assessments start from the simplest scenario (one layer) to complicated ones (two and three layers). The characteristics of the soils and settings for simulation-based optimization are summarized in Table 2. The lower and upper boundaries for k_0 were calculated using the elastic modulus of the soil (unit: MPa, see Equation A4) according to in situ measurements in the sand stratum from Prendergast et al.[22] as follows: [100, 200] for one layer, [100, 500] for two layers, and [100, 500] for three layers. This ensures a large variation of soil properties, so that the true k_0 is located in the defined ranges. The

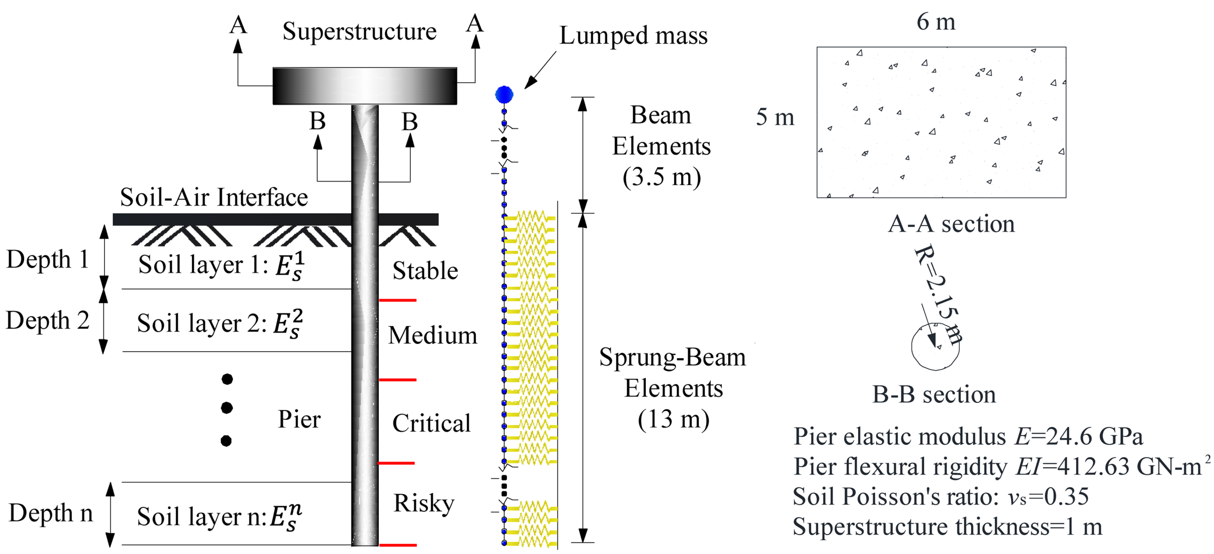

FIGURE 6 Numerical model for a realistic case

TABLE 1 Cases used for simulation-based optimization

Case	Stage	Measurement points: Point 1 Scour depth (m)	Point 1 PNF (Hz)	Point 2 Scour depth	Point 2 PNF	Point 3 Scour depth	Point 3 PNF	Point 4 Scour depth	Point 4 PNF
1	Stable	0.00	7.41	0.10	7.22	0.20	7.12	0.30	7.03
2	Medium	3.40	4.01	3.50	3.95	3.60	3.88	3.70	3.82
3	Critical	6.70	1.84	6.80	1.80	6.90	1.75	7.00	1.71
4	Risky	10.00	0.51	10.10	0.48	10.20	0.46	10.30	0.44

TABLE 2 Settings and results for multilayered soils

Parameter		Soil layer scenario: One layer	Two layers: Layer 1	Two layers: Layer 2	Three layers: Layer 1	Three layers: Layer 2	Three layers: Layer 3
Depth (m)		13	7.1	5.9	3.5	4.5	5
Elastic modulus E_s (MPa)		135	135	202.5	135	202.5	337.5
Initial guess k_0 (MPa)		108.20	126.00		126.00		
Lower boundary k_0		92.60	92.60		92.60		
Upper boundary k_0		196.00	529.46		529.46		
Evaluation number		500	800		800		
True k_0		128.1762	128.1762	198.8717	128.1762	198.8717	345.8670
Predicted k_0	Case 1	128.2287	328.4946	199.0068	253.5750	405.0451	346.0677
	Case 2	128.2299	328.4946	199.0068	253.5750	405.0451	346.0605
	Case 3	128.2304	328.4946	199.0068	253.5750	405.0451	346.0601
	Case 4	128.2304	384.3834	198.8198	101.1529	242.3166	345.9264

initial guess of k_0 was obtained by generating a random number in the defined ranges for practical purposes, which can overcome the uncertainty caused by the effect of the initial guess on the prediction accuracy.

For one soil layer, Figure 7 shows the variation of the objective function value to find the best objective value (i.e., stop criterion) after 500 function evaluations for Case 1. It is seen that the best objective value is below 10^{-5}. In Figure 8, the predicted BSCC for Case 1 almost overlaps with the true solution. Perfect agreements between the predicted BSCCs and the true solution are also observed in Cases 2–4 in Figure 8. Because the soil top surface for Case 2 is at the location where the scour depth is 3.4 m (Point 1 in Table 1), no PNFs will be obtained above Point 1 in Case 2. Thus, the predicted BSCC excludes the segment of the BSCC above that, so is that in Cases 3–4. The coefficient of determination R^2 is nearly equal to 1 in all cases ($R^2 > 0.999999$), which quantitatively confirms the excellent prediction.

This good agreement is also reflected by the comparison between the predicted and true k_0.The predicted value of k_0 in Table 2 is almost the same as the true k_0, and its relative error is about 0.4‰. The results in Figure 8 and Table 2 prove that the predictions of the whole BSCCs for one soil layer using simulation-based optimization are highly accurate.

The predicted values of k_0 for two and three soil layers are also tabulated in Table 2. After 800 function evaluations, the objective value is below 10^{-5}. The predicted values of k_0 for Layer 2 in two soil layers in Cases 1–4 are very close to the true values with a relative error of 0.67‰, while the predicted values of k_0 for Layer 1 are different from the true value to some extent. This phenomenon is also observed in the results for the cases with three soil layers. The predicted values of k_0 for Layer 3 in Cases 1–4 are very close to the true value, while the values differ in Layers 1 and 2. This is possibly caused by the high nonlinearity of the system. Another possible reason is that E_s increases from Layer 1 to the

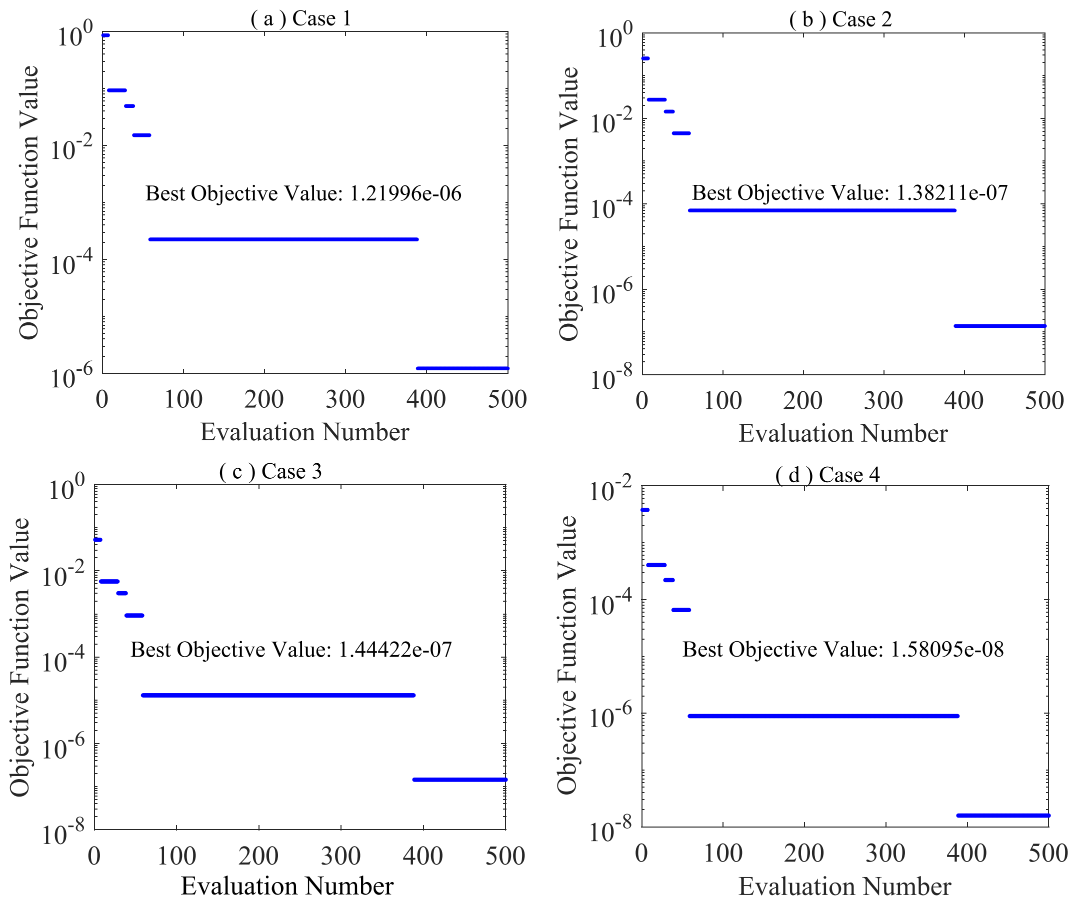

FIGURE 7 Variation of objective function value using simulation-based optimization for one soil layer: (a) Case 1, (b) Case 2, (c) Case 3, and (d) Case 4

FIGURE 8 BSCC predictions for one soil layer

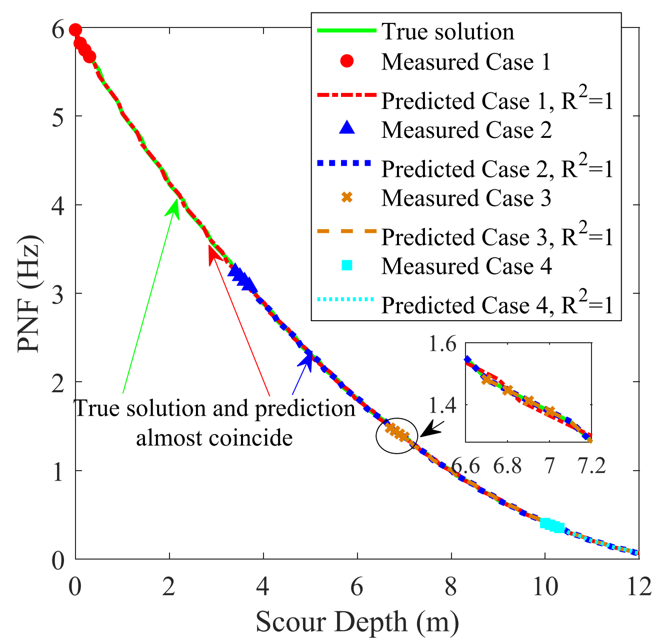

bottom soil layer in the cases with two and three soil layers. E_s determines k_0 (see Equation A4), and the bottom soil layer has the highest value of E_s. Under this condition, the bottom soil will provide much more contribution of the stiffness to the system than the near-surface soil because the PNF mainly depends on the elastic modulus at the bottom[39]

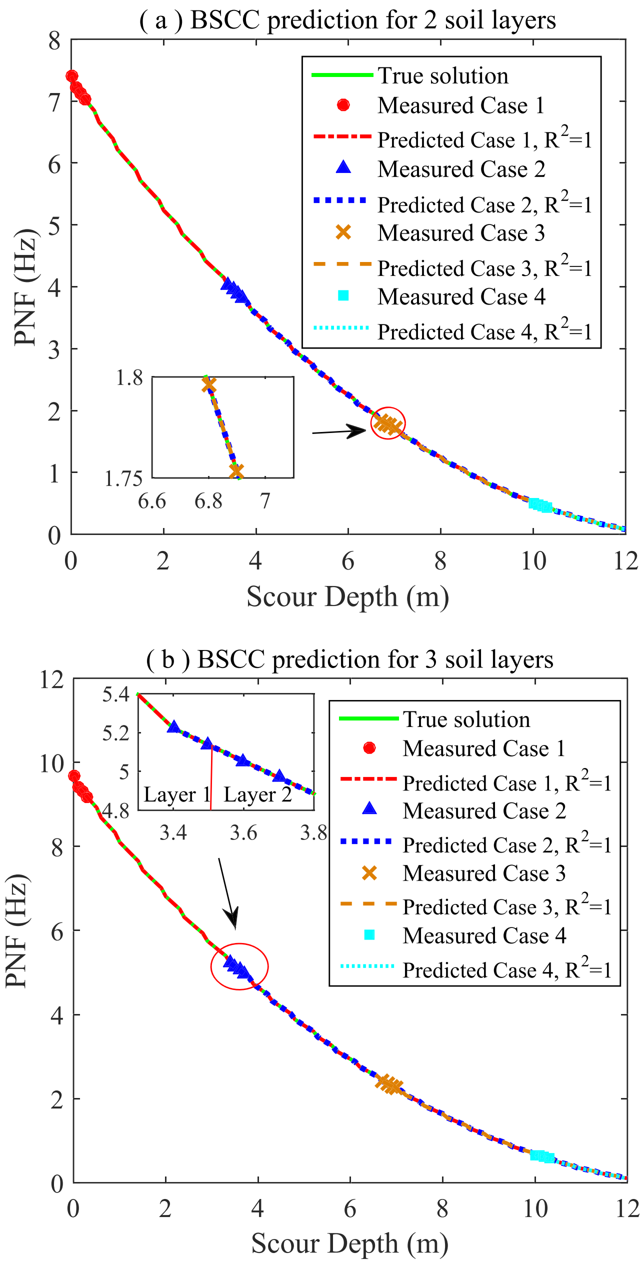

FIGURE 9 BSCC predictions with multilayered soils: (a) two soil layers and (b) three soil layers

(in other words, the PNF is determined by the stiffness of the whole bridge pier–soil system rather the soil component only, so the bottom boundary constraints of the pier by the third soil layer can affect the PNF more significantly than the stiffness contribution from the near-surface soil). Therefore, when the predicted k_0 value in the bottom soil layer is close to the true one, this situation very likely leads to the predicted PNFs comparable to the measured ones, regardless of k_0 values in the near-surface soil layers. However, the predicted whole BSCCs for two and three soil layers are in still good agreement with the true solution, as shown in Figure 9. In the zoom-in view, the predicted BSCCs completely overlap the true solution, regardless of scour depth ranges (scour severity). Moreover, the predicted BSCCs are very smooth at the interface between the two layers (Figure 9b), where k_0 and E_s are discontinuous. For all cases, the coefficient of determination R^2 is extremely close to 1 ($R^2 > 0.999999$). This indicates that the predictions of the whole BSCC with multilayered soils using simulation-based optimization are also highly accurate. Although the predicted values of k_0 for Layer 1 in two soil layers and for Layers 1 and 2 in three soil layers are different from the true solutions, the predicted k_0 value in the bottom soil layer with the proposed approach is close to the true one (see Table 2). As explained above, the contribution of the stiffness from the bottom soil mainly determines the PNF in the BSCC. Thus, the difference in k_0 predictions in the near-surface soil layers does not affect the BSCC prediction accuracy in using the simulation-based optimization approach for PNF–scour detection. The above results were confirmed with more study cases, all of which yielded similar successes. Therefore, we prove that the proposed simulation-based optimization approach is capable and reliable in the prediction of the whole BSCC with multilayered soil conditions in any scour depth ranges, regardless of the scour severity for the measurements and the number of the soil layer.

3.3 | Effect of the number of measurements on prediction accuracy

The effect of the number of measurements on the prediction accuracy is discussed in this subsection. The purpose is to investigate the dependency of the prediction accuracy for k_0 values in the multilayered soils. It is also helpful to examine the accuracy of the whole BSCC prediction using less than four measured points, which is highly desirable from a practical viewpoint.

Two and three soil layer conditions were studied based on the scour condition of Case 1. The number of measurements was considered from 2–15 points with 0.1 scour depth increment that is the same as that in Table 1. Thus, the range of scour depths considered here was 0–1.4 m. As shown in Table 4, increasing the number of available measured points does not lead to more accurate predictions for the values of k_0. However, an interesting finding was obtained in the predictions of BSCCs in Figure 10a,b. The BSCCs predicted with less measured points, that is, two measured points for two soil layers and three measured points for three soil layers, coincide with not only those predictions using more measured points but also the true solution. The true solution in Figure 10 is the same as that in Figure 9 determined using the predetermined k_0 via the testing data explained in Section 3.1. We also evaluated the effect of the measurement number with Cases 2 and 4 for medium and risky scour stages and showed the results in Figure 10c,d. Similarly, the BSCCs predicted with two measured points for two soil layers and three measured points for three soil layers coincide with the true solution. These two figures also plot the predicted BSCCs prior to the initial scour depth, that is, the BSCC part before 3.4 and 10 m for two and three soil layers, respectively. The parts are shown in the figures divided by the vertical dashed line. The good match indicates that the proposed approach is capable of using measurements from the risky scour stage to accurately predict the whole BSCC. The predicted BSCC also includes the range of scour depths for the previous stable scour stage. Figure 10 shows that the whole BSCC can be accurately predicted as long as a given "minimum criterion" is satisfied: the number of measurements needs to be equal to or larger than that of the unknown parameters (i.e., k_0 in each soil layer). Such a finding is useful to guide the proposed approach in practice as the number of needed data points from the field can be reduced if the minimum criterion is satisfied.

TABLE 4 Effect of using the number of measurements on predicted k_0

			Two soil layers		**Three soil layers**		
			k_0 (MPa)		**k_0 (MPa)**		
Parameter			**Layer 1**	**Layer 2**	**Layer 1**	**Layer 2**	**Layer 3**
Evaluation number			800		800		
True value			128.1762	198.8717	128.1762	198.8717	345.867
Predicted value	Case 1	2 points	328.4946	199.0068	-		
		3 points	328.4946	199.0068	253.575	405.0451	346.0674
		4 points	328.4946	199.0068	253.575	405.0451	346.0677
		8 points	328.4946	199.0068	253.575	405.0451	346.0639
		15 points	328.4946	199.0068	253.575	405.0451	346.0626
	Case 2	2 points	328.4946	199.0068	-		
		4 points	328.4946	199.0068			
	Case 4	3 points	-		101.1529	242.3166	345.9264
		4 points			101.1529	242.3166	345.9264

Note: k_0 values here are predicted for each soil layer rather than measurement data points.

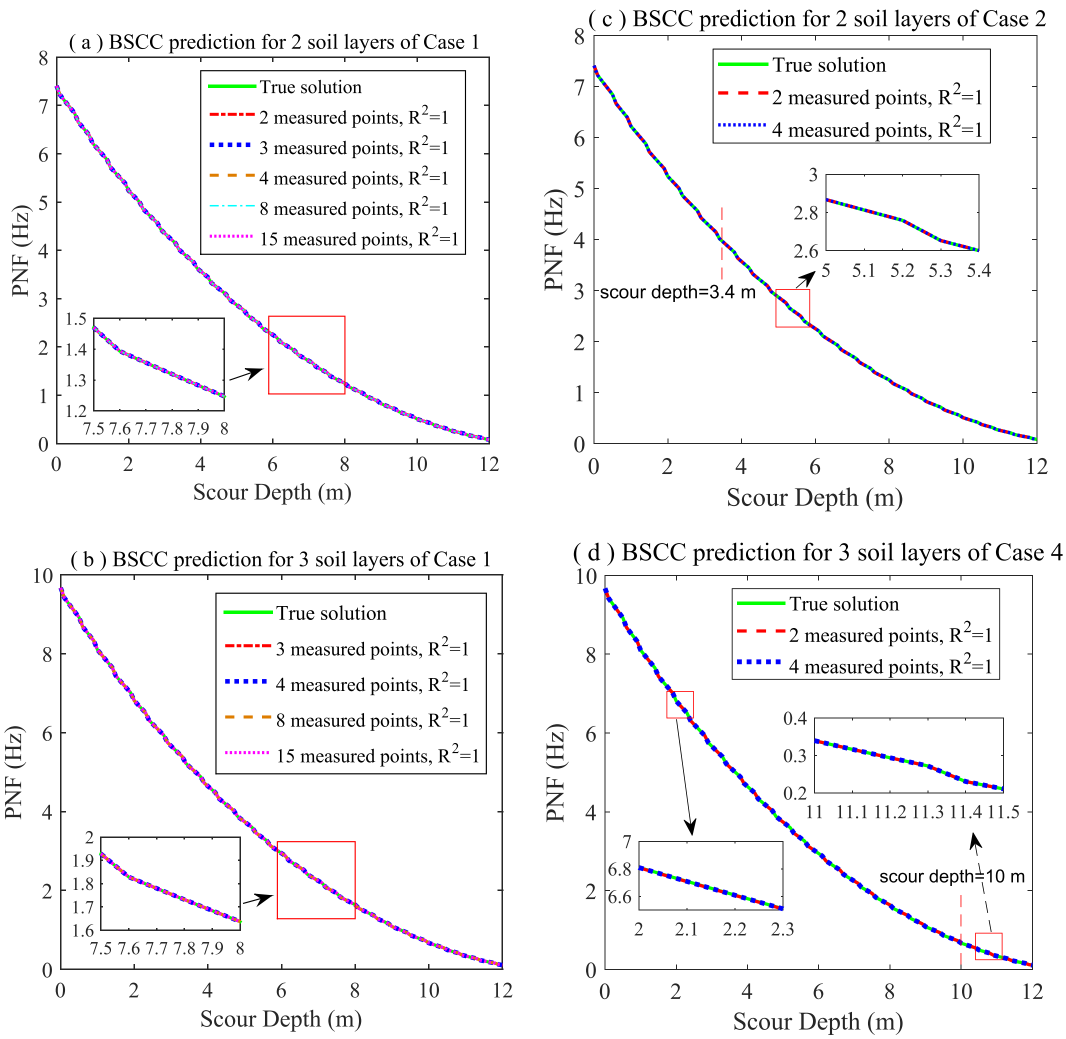

FIGURE 10 Comparison of the BSCC predictions based on different numbers of measurements: (a) two soil layers of Case 1 with 2–15 points, initial scour depth = 0; (b) three soil layers of Case 1 with 2–15 points, initial scour depth = 0; (c) two soil layers of Case 2 with 2–4 points, initial scour depth = 3.4 m; and (d) three soil layers of Case 4 with 2–4 points, initial scour depth = 10 m. Note that the BSCCs before the initial scour depth (i.e., divided by the vertical dashed line) are also plotted in (c) and (d)

3.4 | BSCC prediction considering measurement errors

Errors are inevitable in field measurements. Such errors need to be taken into consideration, so that the proposed simulation-based optimization approach can be a practical tool in real-world scour monitoring applications. In this subsection, we investigate the influence of the errors in the measurements of the PNF and scour depth on the accuracy of the BSCC predictions with the proposed approach.

As for the PNF, Peeters and De Roeck[52] reported 1-year monitoring results of the Z-24 bridge with a main span of 30 m supported by four concrete piers, in which the PNF of the bridge was measured under real environmental effects. According to the results, the standard deviation of 40 plus measured PNFs of this bridge at a temperature of 15°C is 0.0164 Hz for one scour depth. Based on these field results, a standard deviation of 0.0164 Hz was adopted to generate "inaccurate" PNFs for evaluating the performance of the proposed approach. Systematic errors due to inappropriate operations and bad equipment calibrations were not considered here; therefore, the mean of PNFs is equal to the "true" solution calculated with the numerical simulation program detailed in Section 2.2. MATLAB programs were developed to generate random PNFs with such a deviation and the mean value.

To obtain random errors in scour depth measurements, we refer to the recently proposed sensor techniques for measuring scour depths. Here, we take the time domain reflectometry (TRD) sensor for example. The scour depths measured by the TRD sensor has an absolute deviation of 1.5 cm.[5,53] Similar to the PNF, systematic errors that need to be avoided in field measurements were not considered for scour depth measurements. Accordingly, values of scour depths from the numerical simulation were used as the "true" value and consequently the mean of measured scour depths. An absolute deviation of 1.5 cm was utilized to generate measured scour depths with random errors using the MATLAB programs. Six scenarios from light to severe scour conditions were evaluated with two soil layers using three measured data points. The details of randomly generated scour depths and PNFs are tabulated in Table 5.

BSCCs can be predicted at the high accuracy using field measurements with random errors. As shown in Figure 11, the predicted whole BSCCs are in good agreement with the true solution. In zoom-in views, the predicted and actual results are very close for Scenarios 1–3 and 6 in all three local scour depth ranges. There are slight differences between the predicted BSCCs and the true solution for Scenarios 4 and 5. However, this difference is very small. For all the scenarios, the average and maximum differences for scour depths are about 1.5 and 3 cm, respectively.

Table 6 shows the predicted values for two soil layers considering measurement errors tabulated in Table 5. Due to the random deviations, differences between the predicted values and the true values can be observed, which are more significant than those without considering the errors in PNF and scour depth measurements in Table 2. The best objective values of most of the scenarios in Table 6 are higher than 10^{-5}, though the evaluation number increases significantly. However, the good BSCC predictions with field measurement errors in Figure 11 indicate that the proposed simulation-based optimization approach for predicting the whole BSCC can accommodate and even compromise the measurement errors in a very satisfactory way. This fact proves the accuracy, reliability, and flexibility of the proposed approach for field applications. It is worthwhile to mention that the proposed approach is evaluated using the BSCC from 1D sprung-beam simulations of a single pier for simply supported bridges, while the BSCC from 3D simulations

TABLE 5 Scenarios with two soil layers considering measurement errors

Scenario	Random scour depth (m) Point 1	Point 2	Point 3	Random PNF (Hz) Point 1	Point 2	Point 3
1	0	0.1094	0.204	7.4152	7.2207	7.1799
2	0	0.1122	0.1879	7.4365	7.194	7.1666
3	0	0.0888	0.1934	7.3694	7.2084	7.099
4	0	0.1124	0.2014	7.4206	7.2211	7.171
5	3.5094	3.604	3.7137	3.9576	3.8887	3.8775
6	10.0094	10.104	10.2137	0.5141	0.4875	0.4424

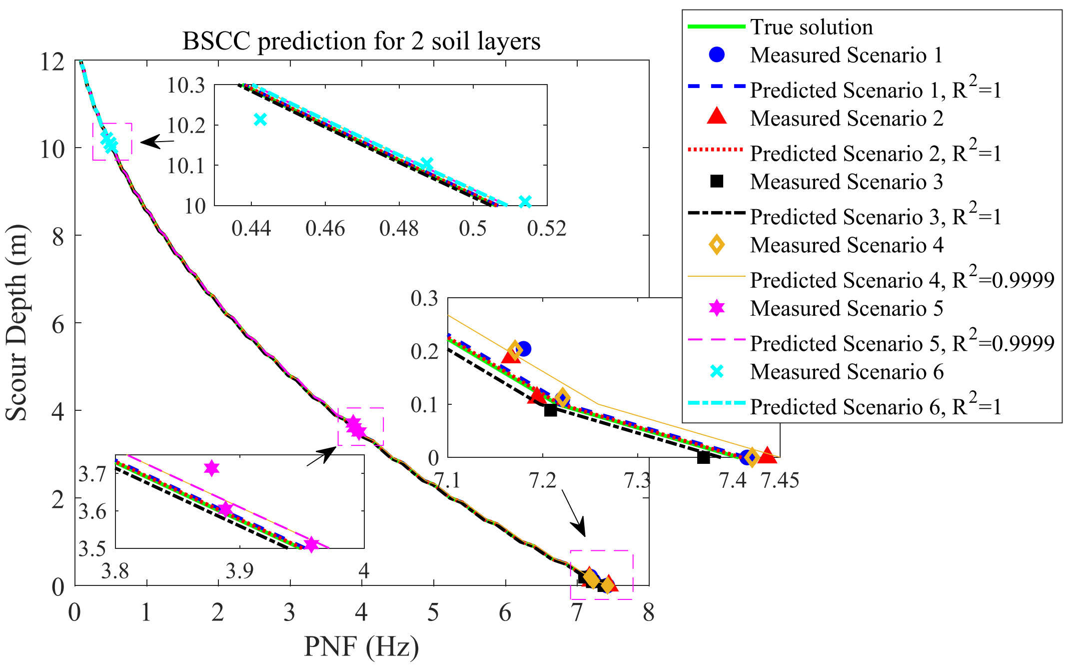

FIGURE 11 BSCC predictions considering measurement errors for two soil layers

TABLE 6 Settings and results for two soil layers considering measurement errors

Parameter	Two soil layers		
	Layer 1	Layer 2	
Evaluation number	2000		
Measurement number	3		
True value	128.1762	198.8717	
	Predicted value		Best function value
Scenario 1	5086.9318	199.3862	2.60E-03
Scenario 2	2283.9951	199.105	3.10E-03
Scenario 3	1256.0351	197.9034	4.76E-04
Scenario 4	944.7371	201.394	2.40E-03
Scenario 5	944.7371	201.394	1.80E-03
Scenario 6	1256.0351	197.9034	3.87E-04

Note: To include all possible k_0 values for all types of soils, the lower and upper boundaries for k_0 in this table are obtained using the elastic modulus of soils (MPa) with [0.1, 5000] for two soil layers.

(e.g., a pier with a group of piles for deep foundations) has not been considered. Further research is thus needed to evaluate the performance of the proposed approach for the 3D simulation BSCC.

4 | CONCLUDING REMARKS

No theory or method is currently available to guide the prediction of scour depths based on measured PNFs. This missing theory or method is a key issue that prevents the wide application of the PNF-based method for bridge scour detection, which is also applicable to the health monitoring of other structures with soil–structure interaction. This study addresses this key issue by presenting a comprehensive investigation into the BSCC including its characteristics, prediction, and application, to enable the PNF-based bridge scour monitoring method in practice.

For the BSCC prediction, we proposed a simulation-based optimization method, in which the whole BSCC, that is, from light to severe scour conditions, can be predicted with a few measured scour depth–PNF data points (e.g., 2–4) within a small scour depth range (e.g., 0.2–0.5 m). This proposed approach integrates the Winkler-based numerical model into a global optimization technique to first predict the modulus of subgrade reaction, which represents the major influence of soils on the dynamic response of the pier but is difficult to obtain at real bridges, and then to predict the whole BSCC to avoid the use of a closed-form BSCC function, which may not exist. The performance of the proposed approach was evaluated using several practical scenarios with realistic multilayered soil conditions. We found that the proposed approach is highly accurate for predicting the whole BSCC with four measured points or even less as long as the "minimum criterion" is satisfied, regardless of the scour severity for the measurements and the number of the soil layer.

For applications, we investigated the influence of random errors in the measurements of the PNF and scour depth on the BSCC prediction. The results indicated that the predicted whole BSCCs are also in good agreement with the true solution. Therefore, the proposed simulation-based optimization approach to predict the BSCC is accurate, capable, and reliable for PNF-based scour monitoring at real bridges. This study provides a solid cornerstone for the maturation of the PNF-based scour monitoring method and other frequency-based structural health monitoring methods involving soil–structure interaction.

ACKNOWLEDGMENTS

We thank the editor and reviewers for their careful reading of the manuscript and their constructive comments.

AUTHOR CONTRIBUTIONS

Ting Bao conceptualized the study, conducted the formal analysis, designed the methodology, prepared the original draft, and reviewed and edited the manuscript. Zhen Liu prepared the resources and reviewed and edited the manuscript.

ORCID

Ting Bao https://orcid.org/0000-0002-2065-7750
Zhen (Leo) Liu https://orcid.org/0000-0001-8013-3804

REFERENCES

1. Wardhana K, Hadipriono FC. Analysis of recent bridge failures in the United States. *J Perform Constr Facil*. 2003;17(3):144-150.
2. Klinga JV, Alipour A. Assessment of structural integrity of bridges under extreme scour conditions. *Eng Struct*. 2015;82:55-71.
3. Azhari F, Loh KJ. Laboratory validation of buried piezoelectric scour sensing rods. *Struct Control Health Monit*. 2017;24(9):1-14.
4. Gee K. National bridge inspection standards scour evaluations and plans of action for scour critical bridges. Washington, DC: Federal Highway Administration; 2008.
5. Yu X, Zhang B, Tao J, Yu X. A new time-domain reflectometry bridge scour sensor. *Struct Health Monit*. 2013;12(2):99-113.
6. Hunt B. NCHRP synthesis 396: Monitoring scour critical bridges. Washington, DC: Transportation Research Board; 2009.
7. Bao T, Liu Z. Vibration-based bridge scour detection: a review. *Struct Control Health Monit*. 2016;24(7):1-19.
8. Foti S, Sabia D. Influence of foundation scour on the dynamic response of an existing bridge. *J Bridge Eng*. 2011;16(2):295-304.
9. Elsaid A, Seracino R. Rapid assessment of foundation scour using the dynamic features of bridge superstructure. *Construct Build Mater*. 2014;50:42-49.
10. Xiong W, Kong B, Tang P, Ye J. Vibration-based identification for the presence of scouring of cable-stayed bridges. *J Aerosp Eng*. 2018;31(2):04018007.
11. Wu B, Chen W, Li H. Real-time monitoring of bridge scouring using ultrasonic sensing technology. Paper presented at: SPIE Smart Structures and Materials & Nondestructive Evaluation and Health Monitoring. San Diego, CA, USA.
12. Chen G, Pommerenke D, Zhou Z, Huang Y, Radchenko A. Inventors; Google Patents, assignee. Sensors for integrated monitoring and mitigation of erosion. 2013.
13. Radchenko A, Pommerenke D, Chen G, et al. Real time bridge scour monitoring with magneto-inductive field coupling. Paper presented at: SPIE Smart Structures and Materials; Nondestructive Evaluation and Health Monitoring. San Diego, CA, USA; 2013:86922A-1-15.
14. Tao J, Yu X, Yu X. Real-time TDR field bridge scour monitoring system. Paper presented at: Structures Congress 2013; Pittsburgh, USA.
15. Dahal P, Peng D, Yang YL, Sharif H. RSS based bridge scour measurement using underwater acoustic sensor networks. *Comm Netw*. 2013;5(3):641-648.
16. Wang K, Lin CP, Chung CC. A bundled time domain reflectometry-based sensing cable for monitoring of bridge scour. *Struct Control Health Monit*. 2019;26(1):1, e2345-14.
17. Feng CW, Huang HY, Ju SH. Integrating finite element method with GAs to estimate the scour depth of bridge. *Int J Res Eng Technol*. 2013;5(4):462-465.
18. Feng CW, Ju SH, Huang HY, Chang PS. Using genetic algorithms to estimate the scour depth around the bridge pier. Paper presented at: 28th International Symposium on Automation and Robotics in Construction. Seoul, Korea; 2011.
19. Zhang X, Chen Y, Yao W. Relationship between bridge natural frequencies and foundation scour depth based on IITD method. *J Appl Sci*. 2013;6(1):102-106.
20. Ju S. Determination of scoured bridge natural frequencies with soil-structure interaction. *Soil Dyn Earthq Eng*. 2013;55:247-254.
21. Briaud JL, Yao C, Darby C, et al. Motion sensors for scour monitoring: laboratory experiments and numerical simulations. Paper presented at: Transportation Research Board (TRB) 89th Annual Meeting 2010; Washington, DC.
22. Prendergast LJ, Hester D, Gavin K, O'Sullivan JJ. An investigation of the changes in the natural frequency of a pile affected by scour. *J Sound Vib*. 2013;332(25):6685-6702.
23. Bao T, Swartz RA, Vitton S, Sun Y, Zhang C, Liu Z. Critical insights for advanced bridge scour detection using the natural frequency. *J Sound Vib*. 2017;386:116-133.
24. Masui Y, Suzuki O. Development of a soundness evaluation system for bridge substructured. *JR East Tech Rev*. 2009;14(14):65-68.
25. Bao T, Liu ZL. Evaluation of Winkler model and Pasternak model for dynamic soil-structure interaction analysis of structures partially embedded in soils. *Int J Geomech*. 2019;20(2):04019167.
26. Chen CC, Wu WH, Shih F, Wang SW. Scour evaluation for foundation of a cable-stayed bridge based on ambient vibration measurements of superstructure. *NDT E Int*. 2014;66:16-27.
27. Li S, He S, Li H, Jin Y. Scour depth determination of bridge piers based on time-varying modal parameters: application to Hangzhou Bay Bridge. *J Bridge Eng*. 2017;22(12):1-13.
28. Prendergast LJ, Hester D, Gavin K. Determining the presence of scour around bridge foundations using vehicle-induced vibrations. *J Bridge Eng*. 2016;21(10):1-14.
29. Van Genuchten MT. A closed-form equation for predicting the hydraulic conductivity of unsaturated soils. *Soil Sci Soc Am J*. 1980;44(5):892-898.
30. Fredlund DG, Xing A. Equations for the soil-water characteristic curve. *Can Geotech J*. 1994;31(4):521-532.
31. Huang HY, Chou WY, Ju SH, Feng CW. Application of finite element method and genetic alogorithems in bridge scour detection. Society for Social Management Systems Internet Journal. Kochi, Japan; 2012.
32. Chen XC, Lai YM. Seismic response of bridge piers on elasto-plastic Winkler foundation allowed to uplift. *J Sound Vib*. 2003;266(5):957-965.

33. Yim CS, Chopra AK. Earthquake response of structures with partial uplift on Winkler foundation. *Earthq Eng Struct Dyn*. 1984;12(2): 263-281.
34. Mylonakis G, Nikolaou A, Gazetas G. Soil-pile-bridge seismic interaction: kinematic and inertial effects. Part I: soft soil. *Earthq Eng Struct Dyn*. 1997;26(3):337-359.
35. Wang L, Ma J, Zhao Y, Liu Q. Refined modeling and free vibration of inextensional beams on the elastic foundation. *J Appl Mech*. 2013; 80(4):1-11.
36. Mostafa YE, Naggar MHE. Dynamic analysis of laterally loaded pile groups in sand and clay. *Can Geotech J*. 2002;39(6):1358-1383.
37. Dutta SC, Roy R. A critical review on idealization and modeling for interaction among soil-foundation-structure system. *Comput Struct*. 2002;80(20):1579-1594.
38. Wang S, Kutter BL, Chacko MJ, Wilson DW, Boulanger RW, Abghari A. Nonlinear seismic soil-pile structure interaction. *Earthq Spectra*. 1998;14(2):377-396.
39. Bao T, Liu Z, Bird K. Influence of soil characteristics on natural Frequency-based bridge scour detection. *J Sound Vib*. 2019;446:195-210.
40. Gosavi A. *Simulation-Based Optimization*. Springer; 2003.
41. Mattsson H, Klisinski M, Axelsson K. Optimization routine for identification of model parameters in soil plasticity. *Int J Numer Anal Methods Geomech*. 2001;25(5):435-472.
42. Zhang Y, Gallipoli D, Augarde C. Simulation-based calibration of geotechnical parameters using parallel hybrid moving boundary particle swarm optimization. *Comput Geotech*. 2009;36(4):604-615.
43. Jeong M, Choi JH, Koh BH. Performance evaluation of modified genetic and swarm-based optimization algorithms in damage identification problem. *Struct Control Health Monit*. 2013;20(6):878-889.
44. Sbarufatti C. Optimization of an artificial neural network for fatigue damage identification using analysis of variance. *Struct Control Health Monit*. 2017;24(9):1, e1964-17.
45. Martí R. Multi-start methods. In: *Handbook of Metaheuristics*. Springer; 2003:355-368.
46. Ugray Z, Lasdon L, Plummer J, Glover F, Kelly J, Martí R. Scatter search and local NLP solvers: a multistart framework for global optimization. *INFORMS J Comput*. 2007;19(3):328-340.
47. Horst R, Tuy H. *Global Optimization: Deterministic Approaches*. Springer Science & Business Media; 2013.
48. Cao S, Yuan W. Modified generalized pushover analysis for estimating longitudinal seismic demands of bridges with elevated pile foundation systems. *Lat Am J Solids Struct*. 2014;11(14):2696-2712.
49. Mueller DS, Wagner CR. Field observations and evaluations of streambed scour at bridges. McLean, VA: Research, Development, and Technology Turner-Fairbank Highway Research Center, US Department of Transportation; 2005.
50. CDOESTO. Bridge design practice. Sacramento, CA: Caltrans Division of Engineering Services Technical Organization, California Department of Transportation; 2015.
51. Ashford SA, Juirnarongrit T. Evaluation of pile diameter effect on initial modulus of subgrade reaction. *J Geotech Geoenviron Eng*. 2003; 129(3):234-242.
52. Peeters B, De Roeck G. One-year monitoring of the Z 24-Bridge: environmental effects versus damage events. *Earthq Eng Struct Dyn*. 2001;30(2):149-171.
53. Yu X, Yu X. Laboratory evaluation of time-domain reflectometry for bridge scour measurement: comparison with the ultrasonic method. *Adv Civ Eng*. 2010;2010:1-12.
54. Teh C, Houlsby G. An analytical study of the cone penetration test in clay. *Geotechnique*. 1991;41(1):17-34.
55. Lunne T, Robertson P, Powell J. *Cone Penetration Testing in Geotechnical Practice*. American Society of Civil Engineers (ASCE); 1997.
56. Robertson PK, Campanella R. Interpretation of cone penetration tests. Part I: sand. *Can Geotech J*. 1983;20(4):718-733.
57. Luna R, Jadi H. Determination of dynamic soil properties using geophysical methods. Paper presented at: the First International Conference on the Application of Geophysical and NDT Methodologies to Transportation Facilities and Infrastructure-Geophysics. ST. Louis, MO, USA; 2000.
58. Andrus RD, Stokoe KH II. Liquefaction resistance of soils from shear-wave velocity. *J Geotech Geoenviron Eng*. 2000;126(11):1015-1025.

How to cite this article: Bao T, Liu Z(L). Bridge scour characteristic curve for natural frequency-based bridge scour monitoring using simulation-based optimization. *Struct Control Health Monit*. 2021;28:e2773. https://doi.org/10.1002/stc.2773

APPENDIX A.

A.1 | Taylor series expansion approximation

Applying the Taylor series expansion to the second and fourth derivatives of U and neglecting the transaction errors, we obtain

$$U'''' \approx \frac{U_{i-2} - 4U_{i-1} + 6U_i - 4U_{i+1} + U_{i+2}}{\Delta x^4}, \tag{A1}$$

$$U'' \approx \frac{U_{i-1} - 2U_i + U_{i+1}}{\Delta x^2}. \tag{A2}$$

A.2 | Soil stiffness determination

Accurate acquisition of the soil stiffness is critical to the accuracy of the numerical analysis of the soil-pier interaction. According to Prendergast et al.,[22] the small-strain stiffness method yielded good results for determining the soil stiffness. The soil elastic modulus E_s is the critical parameter for dynamic analyses on the small-strain level. Many ways are available for obtaining E_s, such as the cone penetration test[54–56] via measuring the cone tip resistance and the geophysical method[57,58] via measuring the shear wave velocity of the soil. These tests first obtain the shear modulus G_s (N/m^2) of a soil in the measured area. Then, E_s can be computed from G_s using the following expression[57]:

$$E_s = 2G_s(1+\nu_s), \tag{A3}$$

where ν_s is the small-strain Poisson's ratio of the soil and assumed to be a constant in this study. The relationship between the modulus of subgrade reaction k_0 and the material properties in the Winkler spring method[51] is given by Equation A4:

$$k_0 = \frac{1.0E_s}{1-{\nu_s}^2}\left[\frac{E_s {D_p}^4}{EI}\right]^{1/12}, \tag{A4}$$

where D_p is the pier diameter (m) and EI is the flexural rigidity of the pier (kN/m^2). The lateral spring stiffness therefore can be determined by multiplying k_0 (kN/m^2) with the spacing of the adjacent springs.